RSC Advances

PAPER

View Article Online
View Journal | View Issue

Cite this: *RSC Adv.*, 2022, **12**, 9933

Nano-silver functionalized spherical activated carbon with enhanced dipropyl sulfide adsorption capacity and antibacterial properties†

Zhilian Yang, Tianhao Zhang, Jiarui Ren, Jiawen Li, Jianlong Ge,* Haoru Shan, Tao Ji, Mingshen Xu and Qixia Liu*

Received 8th January 2022
Accepted 13th March 2022

DOI: 10.1039/d2ra00124a

rsc.li/rsc-advances

Owing to the large dynamic adsorption performance and excellent mechanical strength, spherical activated carbon (SAC) has been widely applied in the field of biochemical protection. However, the adsorbed chemical warfare agent molecules might easily escape from the pores of SAC due to the impact of ambient temperature and humidity, resulting in secondary pollution. Herein, to improve the adsorption performance of SAC, an excessive impregnation method was used to fabricate nano-silver functionalized spherical activated carbon (Ag-SAC). The surface physicochemical structure of the obtained Ag-SAC was extensively studied, and dipropyl sulfide (DPS), a simulant of sulfur mustard (HD), was employed as the adsorbate to evaluate its adsorption capability. The effects of $AgNO_3$ impregnation concentration, reaction time, initial concentration and temperature on the adsorption performance, were investigated. The equilibrium adsorption capacity of Ag-SAC towards DPS increased by 13.41% compared with that of pristine SAC. Kinetic models, adsorption isotherm models, and adsorption thermodynamics were used to study the adsorption mechanism. The results revealed that the adsorption of DPS by Ag-SAC is a mixed synergistic process, which includes chemical adsorption and physical adsorption. Moreover, the Ag-SAC exhibited good antibacterial characteristics, with an antibacterial rate over 99.28% against *Escherichia coli*. We anticipate that the Ag-SAC could be a promising material for the development of high performance breathable biochemical protection clothing.

1 Introduction

From 1980 through 1988, sulfur mustard (HD) was employed as a chemical warfare agent in the Iran-Iraq War.[1] Anthrax terrorist attacks and castor toxin events happened in the United States between 2001 and 2004.[2] Despite the establishment of the Biological Weapons Convention (BWC) and the Biological and Toxin Weapons Convention (BTWC) in recent years, certain governments have continued to develop, store, and use biochemical warfare agents, which makes biochemical terrorist attacks a potential threat.[2]

As an effective individual biochemical protection strategy, biochemical protective clothing has been consistently developed to protect medical staff, military people, and firefighters exposed to contaminated environments. Biochemical protective clothing is now classified into two categories based on the protection method, which are barrier and breathable. Although barrier biochemical protective clothing may isolate biochemical warfare agents effectively, its dense structure prevents moisture vapor from escaping, resulting in poor heat-moisture comfort and inability to work for an extended period of time for the wearer.[3] Breathable biochemical protective fabric offers a high moisture vapor transmission rate, providing the wearer with increased comfort and mobility.[3,4] The breathable biochemical protective fabric is usually designed into a multi-layer composite fabric with an activated carbon material as the core adsorption layer.[5,6] Among various activated carbon adsorption materials, spherical activated carbon (SAC) is considered to be one of the promising adsorption materials in the field of biochemical protection due to its excellent mechanical strength, good washing resistance, favorable thermal stability, outstanding chemical resistance, and large dynamic adsorption capacity toward chemical warfare agents.[7] The common SAC materials defend against biochemical agents through physical adsorption. However, due to the impact of ambient temperature and humidity, the adsorbed biochemical agent molecules might easily escape from pores, resulting in secondary pollution.[8] As a result, functionalized SAC materials with high adsorption capacity as well as strong binding affinity are urgently needed.

Related studies have shown that the adsorption and catalytic degradation performance of carbon materials toward

---

National & Local Joint Engineering Research Center of Technical Fiber Composites for Safety and Health, School of Textile and Clothing, Nantong University, Nantong 226019, China. E-mail: gejianlong@ntu.edu.cn; lqx@ntu.edu.cn

† Electronic supplementary information (ESI) available. See DOI: 10.1039/d2ra00124a

chemical warfare agents can be improved by loading appropriate metals on the surface.[9,10] A typical example is that transition metals such as zinc, copper, molybdenum, vanadium and chromium are loaded on carbon materials, resulting in enhanced adsorption capacities for chemical warfare agents like soman, sarin, and mustard gas.[11–13] In recent years, nano-silver has received much concern as a functional material in the field of biochemical protection and detection due to their non-toxic, catalytic and electrochemical properties.[14–16] Furthermore, due to their strong antibacterial performance against bacteria, fungus, and viruses, nano-silver can also be used as an antibacterial material in biological warfare defense.[17–20] Therefore, the loading of nano-silver onto carbon materials was proposed to further increase their adsorption capacity and biochemical protection performance, which is yet to be studied.

In this work, nano-silver loaded spherical activated carbon (Ag-SAC) composites were prepared *via* an excessive impregnation method. The obtained Ag-SAC exhibited a highly microporous pore structure, and nano-silver particles were uniformly loaded on the surface of Ag-SAC. As a result, the Ag-SAC possessed more reaction sites for adsorption interaction, contributing to an enhanced adsorption capacity for the chemical warfare agent simulant. Meanwhile, a possible mechanism was proposed to explain the synergistic effect of chemical adsorption and physical adsorption of Ag-SAC. With the merit of nano-silver, Ag-SAC possessed a satisfactory antibacterial capability. Moreover, the composite fabric made from Ag-SAC and commercial polyester fabric exhibited intriguing water vapor permeability and washing resistance fastness performance. Consequently, the Ag-SAC showed great potential for the application of high performance breathable biochemical protective clothing.

2 Experimental

2.1 Materials

The SAC was purchased from the Kureha Corporation (Japan). Nitric acid was produced by Sinopharm Chemical Reagent Co., Ltd. $AgNO_3$ was obtained from Shanghai Institute of Fine Chemical Materials. Sulfur mustard simulant dipropyl sulfide (DPS) and anhydrous ethanol are purchased from Shanghai MackLin Biochemical Technology Co., Ltd. The above chemicals are analytically pure and directly used without further purification. Polyester fabric was purchased from Zhejiang Duoyi Trade Co., Ltd. Adhesive was purchased from Beijing Huamaoda Technology Co., Ltd.

2.2 Preparation of Ag-SAC

As shown in Fig. 1, the SAC was put into deionized water and boiled for 120 min to remove impurity metals and ash. After that, 10 g of the cleaned SAC and 100 mL of 2 mol L^{-1} nitric acid solution were put in a conical flask and oscillated at 60 °C for 120 min. After the solution was cooled to room temperature, the SAC was rinsed to neutral with deionized water and dried to obtain the pre-oxidized SAC. Afterwards, a series of Ag-SAC composites were prepared by an excessive impregnation method. For the fabrication of Ag-SAC, 5 g of pre-oxidized SAC was immersed in $AgNO_3$ solutions of different concentrations (0.05 mol L^{-1}, 0.5 mol L^{-1} and 1 mol L^{-1}). After ultrasonic treatment for 30 min, the reaction system was placed in a constant temperature oscillator and oscillated at 30 °C for 360 min. Then the obtained sample was filtered and dried completely in a vacuum environment. The following calcination was carried out in a nitrogen atmosphere at 400 °C for 240 min. Finally, the calcinated samples was washed 3–5 times with deionized water to remove excess metal particles. The obtained

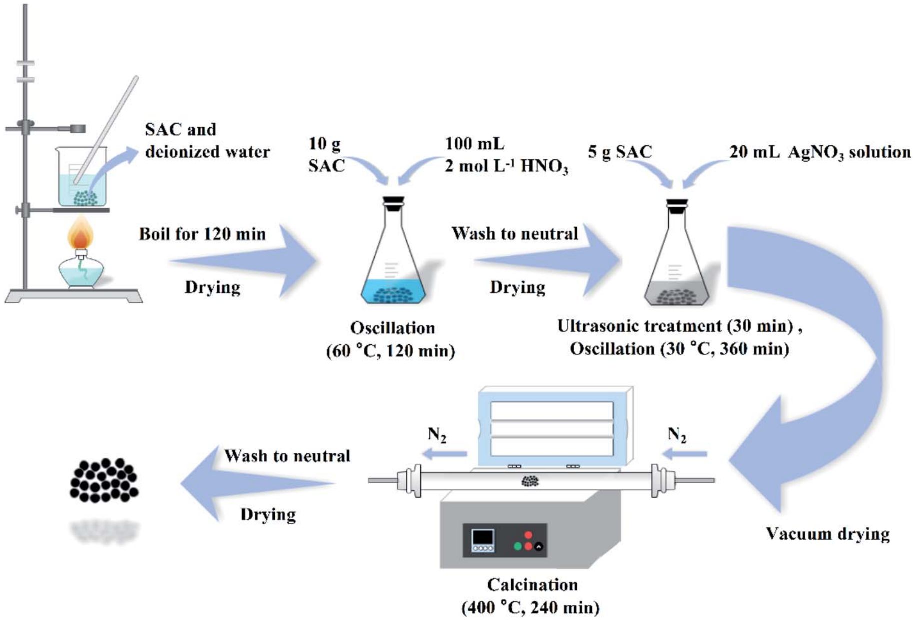

Fig. 1 Schematic diagram of the preparation of Ag-SAC.

Ag-SAC samples were denoted as 0.05M-Ag-SAC, 0.5M-Ag-SAC and 1M-Ag-SAC according to the $AgNO_3$ solutions concentrations, respectively.

2.3 Preparation of composite fabric

Firstly, the adhesive is evenly spread on the polyester fabric in a pointlike manner. Then, Ag-SAC was bonded to polyester fabric to obtain composite fabric. The composite fabric was heated at 80 °C for 1 h and then placed at room temperature for 24 h. The preparation process of composite fabric is shown in Fig. S1.†

2.4 Characterization

The surface morphology and element distribution of the as-prepared Ag-SAC samples were characterized by a scanning electron microscope (SEM, JSM-6510, JEOL, JPN) equipped with an energy dispersive spectrometer (EDS, X-act, Oxford, UK). The specific surface area and pore structure were characterized by automatic physical adsorption analyzer (ASAP 2020, Micromeritics, USA) at 77 K after degassing at 350 °C for 4 h. The specific surface area (S_{BET}) was calculated by the Brunauer–Emmett–Teller (BET) equation, the total pore volume (V_P) was determined at $P/P_0 = 0.98$, the average pore diameter ($4\ V\ A^{-1}$ by BET) was determined by the Barrett–Joyner–Halenda method, and the pore size distributions were calculated by the density functional theory (DFT) method. An X-ray diffractometer (XRD, Ultima IV, Rigaka, JPN) with a Cu Kα radiation source generated at 40 kV and 40 mA was used to verify the crystal structure and phase compositions of the obtained Ag-SAC samples. The surface functional groups were characterized by Fourier transform infrared spectrometers (FT-IR, TENSOR 27, BRUKER, GER). X-ray photoelectron spectroscopy (XPS, K-Alpha+, Thermo Scientific, USA) and Raman spectroscopy (Raman, Horiba HR800, FRA) were used to examine the surface chemical compositions. The antibacterial activity of Ag-SAC samples was evaluated according to Chinese standard GB/T 20944.3-2008 Textiles-Evaluation for antibacterial activity-Part 3: Shake flask method.[21] The water vapor permeability (WVP) tester (W3-031, Labthink, CHN) was used to test the moisture permeability of composite fabric. The washing resistance fastness performance of composite fabric was tested by a washing fastness testing machine according to Chinese standard GB/T 29255-2012 Textiles-Tests for colour fastness-colour fastness to domestic and commercial laundering using a non-phosphate reference detergent incorporating a low-temperature bleach activator.

2.5 Sulfur mustard simulant adsorption experiments

Due to its ease of manufacture, storage, and high destructiveness, sulfur mustard is one of the most dangerous chemical agents.[22,23] Dipropyl sulfide (DPS) with similar physical and chemical qualities is a frequently-used simulant of sulfur mustard for experimental research. Batch adsorption experiments were conducted to investigate the adsorption property of Ag-SAC against DPS. Anhydrous ethanol was chosen as the solvent.[24] 0.04 g adsorbents were added into 30 mL DPS–ethanol solution in a conical flask and shaken at 180 rpm in a constant temperature oscillator. The initial DPS concentration of the solution was adjusted from 40 to 90 mg L^{-1} by changing the ratio of DPS and anhydrous ethanol. Besides, the temperature of the adsorption system was varied (30 °C, 40 °C, 50 °C, and 60 °C) to study the influence of temperature on adsorption performance. The concentration of DPS in the solution was measured by analyzing the supernatant at predetermined time

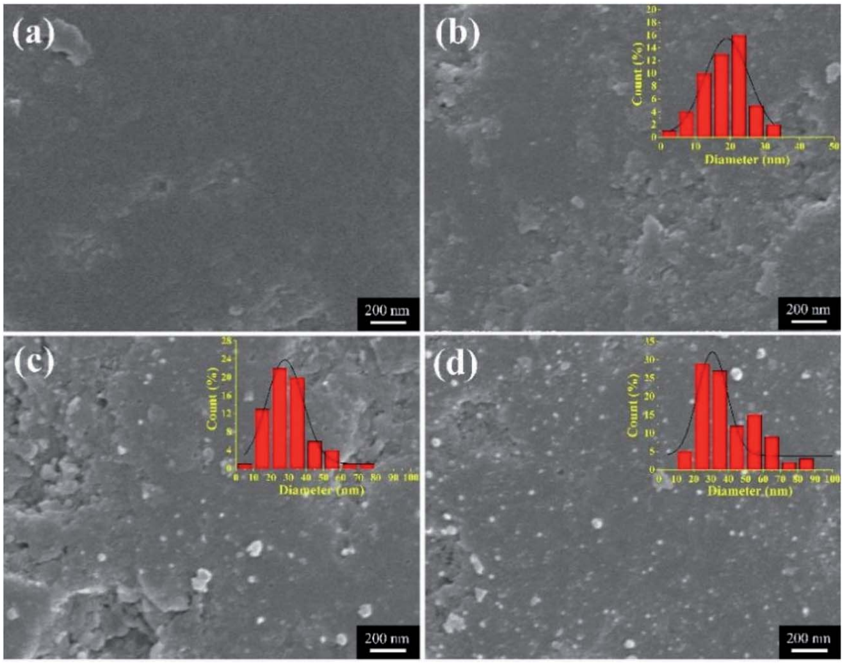

Fig. 2 SEM images of SAC and various Ag-SAC samples: SAC (a); 0.05M-Ag-SAC (b); 0.5M-Ag-SAC (c); 1M-Ag-SAC (d).

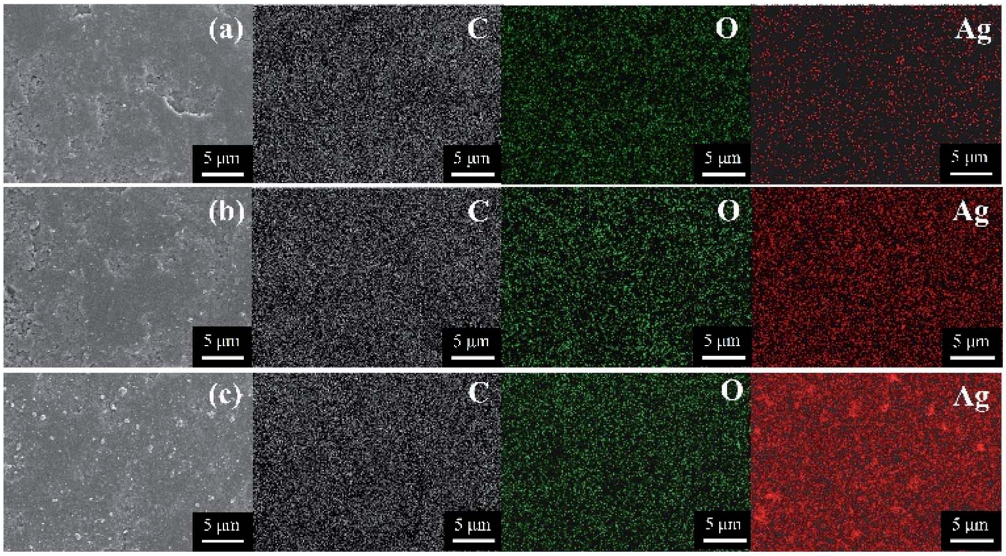

Fig. 3 Element mapping images of various Ag-SAC samples: 0.05M-Ag-SAC (a); 0.5M-Ag-SAC (b); 1M-Ag-SAC (c).

intervals using a UV-visible spectrophotometer (TU-1900, Beijing Purkinje General Instrument Co., Ltd.) at 208 nm. The adsorption capacity at equilibrium, q_e (mg g^{-1}) was calculated as follows:

$$q_e = \left(\frac{C_0 - C_e}{W}\right) \times V \tag{1}$$

where C_0 and C_e are the initial and equilibrium DPS concentration in the solution, respectively, W (g) is the mass of adsorbent, and V (L) is the volume of solution.

The adsorption capacity of Ag-SAC at q_t (mg g^{-1}) of t (min) was calculated by the following equation:

$$q_t = \left(\frac{C_0 - C_t}{W}\right) \times V \tag{2}$$

where C_t (mg L^{-1}) is the solution concentration at t.

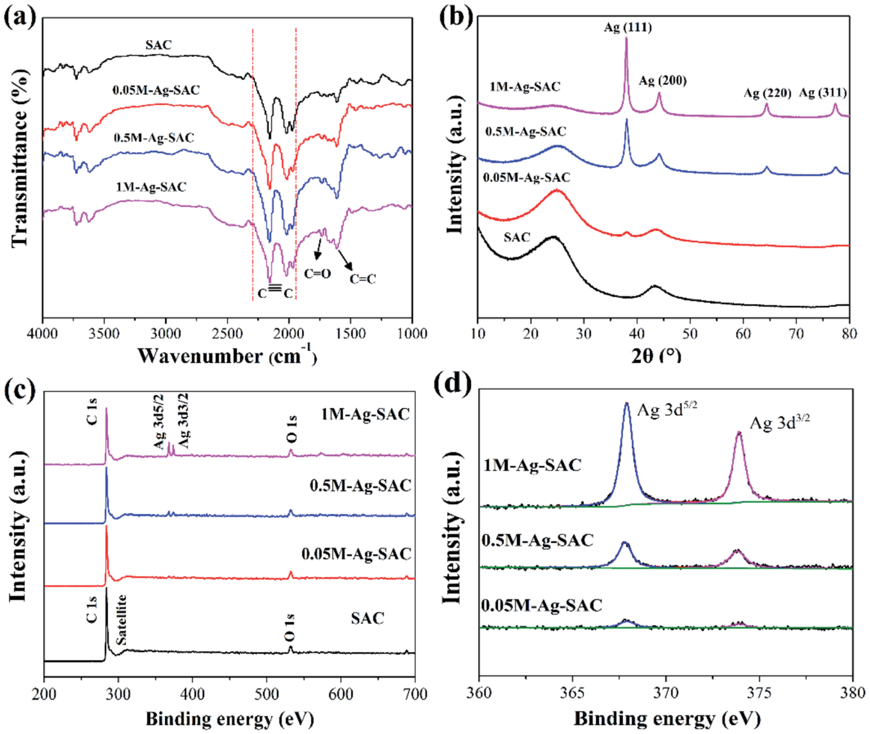

Fig. 4 FT-IR spectra (a) and XRD patterns (b) of SAC and various Ag-SAC samples; XPS survey spectra of SAC and various Ag-SAC samples (c); high resolution Ag 3d spectra of various Ag-SAC samples (d).

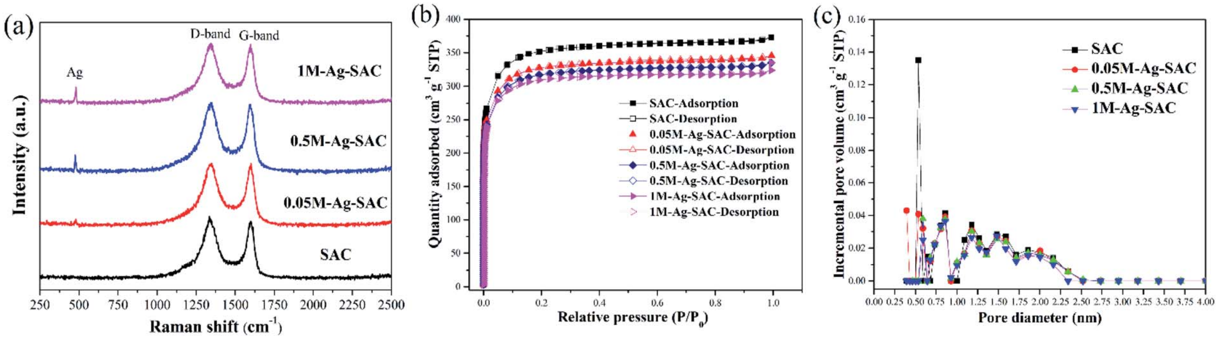

Fig. 5 Raman spectra (a) of SAC and various Ag-SAC samples; N_2 adsorption isotherms (b) and pore size distribution (c) of SAC and various Ag-SAC samples.

3 Results and discussion

3.1 Characterization of Ag-SAC samples

The micro surface morphologies of pristine SAC and Ag-SAC samples were observed *via* SEM. As shown in Fig. 2(a)–(d), unlike the surface of pristine SAC, the surface of Ag-SAC exhibits randomly distributed depressions of various scales, as well as many etched pores and channels in the interior structure of these depressions. Due to the oxidation etching impact of nitric acid, the pores on the Ag-SAC surface began to collapse and certain pores progressively expanded.[25]

The nanoparticles loaded on the Ag-SAC surface shows an average size of 20–30 nm (Fig. 2(b)–(d)). As shown in Fig. 2(c) and (d), nanoparticles bigger than 80 nm were also observed on the surfaces of 0.5M-Ag-SAC and 1M-Ag-SAC, demonstrating that the $AgNO_3$ concentration had a significant impact on the size of nanoparticles. Elemental mapping images shown in Fig. 3 indicated that the distribution of Ag on the surface of 0.05M-Ag-SAC and 0.5M-Ag-SAC is quite uniform, and the weight ratios of Ag elements rise as the $AgNO_3$ concentration increases (Table S1†). Meanwhile, some dense region of Ag appeared on the surface of 1M-Ag-SAC, which may be attributed to the aggregation of Ag at the high $AgNO_3$ concentration. The FT-IR spectra of pristine SAC and various Ag-SAC samples are shown in Fig. 4(a). The peak at 1620 cm^{-1} corresponds to the C$=$C stretching vibration in materials.[26] The stretching vibration of the alkynyl group (C$\equiv$C) was responsible for the spectral area of 2220 cm^{-1}.[27] Compared with SAC, the intensity of the characteristic peak corresponding to the C$=$O vibration of Ag-SAC at 1730 cm^{-1} increased,[28] which proved that the surface acidity of Ag-SAC was enhanced. The XRD patterns of SAC and Ag-SAC samples are shown in Fig. 4(b). It can be found that the XRD patterns of Ag-SAC exhibit characteristic diffraction peaks at 38°, 45°, 65° and 78°, which correspond to the (111), (200), (220) and (311) facets of the face-centered cubic (fcc) crystal structure of silver, respectively,[29] proving that nano-silver was successfully loaded on the surface of Ag-SAC. The wide XRD peak at 25.8° assigned to the diffraction of amorphous carbon remain unchanged before and after treatment, indicating that the treatment process has no effect on the crystal structure of carbon.[30]

The chemical structure and elemental composition of SAC and Ag-SAC were further analyzed by XPS analysis. Fig. 4(c) shows the survey spectra of SAC and Ag-SAC, and Fig. 4(d) shows the high resolution Ag 3d spectra of Ag-SAC. The XPS survey spectra in Fig. 4(c) indicate that the predominant surface elements of both SAC and Ag-SAC are carbon and oxygen with the significant C 1s and O 1s peaks at 284 eV and 530 eV, respectively.[31] Obvious Ag 3d peaks were also observed in the spectra, further confirming the successful loading of nano-silver on the surface of Ag-SAC. The peaks at 368.1 eV and 374.1 eV in Fig. 4(d) correspond to the valence states of Ag $3d_{5/2}$ and Ag $3d_{3/2}$ of nano-silver, respectively.[32] The spin energy separation of 6.0 eV further confirmed that metallic silver (Ag^0) exists on the surface of Ag-SAC in the reduced form.[31] The intensity of the Ag 3d absorption peak increases with the increase of silver nitrate concentration, which indicates that the concentration of silver nitrate has a great influence on the content of nano-silver on the Ag-SAC surface, which is consistent with the above conclusion.

Fig. 5(a) shows the Raman spectra of the Ag-SAC in the Raman shift range of 250–2500 cm^{-1}. The peaks at 1350 cm^{-1} and 1600 cm^{-1} ascertained as the amorphous D-band peak and polycrystalline G-band peak of activated carbon can be obviously observed.[33] The amorphous D-band peak and polycrystalline G-band peak reflect the disordered carbon and graphitic of the Ag-SAC surface, respectively.[34] In addition, an absorption peak of Ag appeared at 500 cm^{-1}, indicating that nano-silver were formed on the surface of Ag-SAC.[35] Besides, the almost unchanged characteristic of D-band peak and G-band peak with the increment of nano-silver loading amount, indicated that addition of nano-silver had tiny effect on the carbonaceous structures of Ag-SAC.

Table 1 Porous texture parameters of SAC and various Ag-SAC samples

Samples	S_{BET} (m^2 g^{-1})	V_p (cm^3 g^{-1})	L (nm)
SAC	1077.84	0.58	2.14
0.05M-Ag-SAC	998.08	0.53	2.14
0.5M-Ag-SAC	968.91	0.52	2.13
1M-Ag-SAC	945.17	0.50	2.12

Fig. 5(b) shows the N_2 adsorption–desorption isotherms of SAC and Ag-SAC at 77 K. The results show that both SAC and Ag-SAC exhibit a type I adsorption–desorption isotherm. The pore volume was rapidly filled below a relative pressure of about 0.1, and kept almost constant at higher relative pressure, indicating that both SAC and Ag-SAC are highly microporous. Small adsorption hysteresis was observed at higher relative pressure ($0.45 \leq P/P_0 \leq 0.95$) for all samples, indicating that a small amount of mesopores also exist. When the relative pressure reaches 0.95, the nitrogen adsorption amount increases slightly, which may be caused by the adsorption of macropores. Compared with SAC, the nitrogen adsorption capacity of Ag-SAC samples were decreased and the decline degree increases with increasing the $AgNO_3$ solution concentration. The detailed porous texture parameters of SAC and Ag-SAC are shown in Table 1 and Fig. 5(c). As shown in Table 1, in line with nitrogen adsorption amount, the BET surface area and total pore volume of Ag-SAC samples also decreased with an increase in the concentration of $AgNO_3$ solution, which can be attributed to the blockage of some pores due to the formation of nano-silver crystals.[36,37]

3.2 Sulfur mustard simulant adsorption performance by Ag-SAC

3.2.1 Effect of reaction time and initial concentration. The Ag-SAC composites were employed as an adsorbent to adsorb DPS in order to assess its application potential in the field of biochemical protection. Fig. 6(a) shows the effect of reaction time on adsorption capacity of SAC and Ag-SAC toward DPS. The effect of initial concentration on adsorption capacity of Ag-SAC toward DPS are shown in Fig. 6(b). It can be seen from Fig. 6(a) that all Ag-SAC samples show a larger DPS adsorption capacity than SAC with an equilibrium adsorption capacity of 30.28 mg g^{-1}. It can be calculated that the equilibrium adsorption capacity of the optimum 0.5M-Ag-SAC sample increases by 13.41%. However, as mentioned above, the loading of nano-silver leads to a decrease in specific surface area and pore volume of Ag-SAC, indicates that SAC has better physical adsorption properties than Ag-SAC.[38] Therefore, the increased DPS adsorption capacity of Ag-SAC is most likely caused by an adsorption performance dominated by chemical adsorption. To further explore the adsorption mechanism of Ag-SAC, the adsorption experiment was carried out with 0.5M-Ag-SAC as the adsorbent to examine the impact of the initial concentration of DPS on the adsorption performance. As shown in Fig. 6(b), with the increase of initial concentration, the adsorption capacity of Ag-SAC increased first and then decreased slowly. When the initial concentration was 60 mg L^{-1}, the equilibrium adsorption capacity was the largest. This is because the concentration gradient provides the main driving force for Ag-SAC to adsorb DPS.[39]

3.2.2 Adsorption kinetics. Adsorption behavior is a complex process, including external liquid film-diffusion, surface adsorption and intra-particle diffusion. In order to further understand the adsorption mechanism of DPS on Ag-SAC, three different adsorption kinetic models such as the pseudo-first-order model, the pseudo-second-order model, and the intra-particle diffusion model were used to study the adsorption process, as shown in Fig. 7.

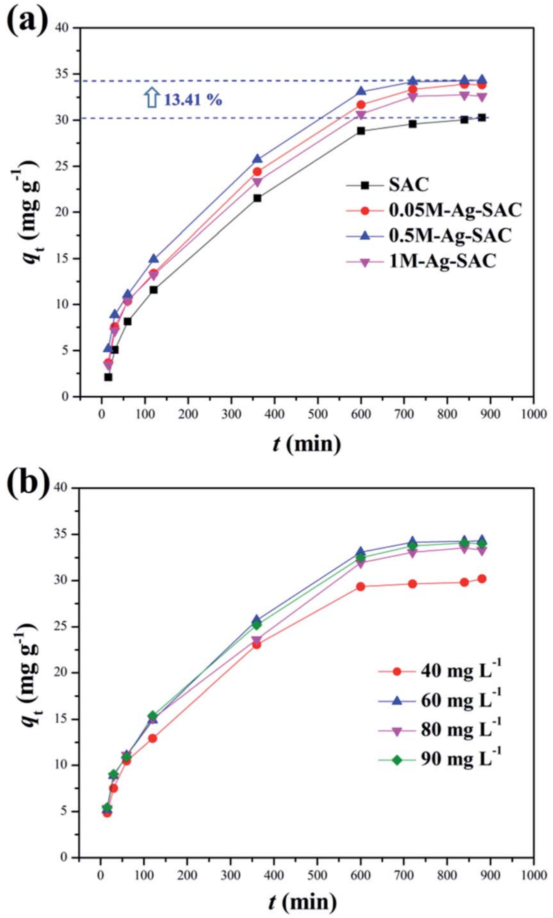

Fig. 6 Effect of reaction time on adsorption capacity of SAC and Ag-SAC toward DPS (a) (C_0 = 60 mg L^{-1}, dosage = 0.8 mg mL^{-1}, temperature = 30 °C); effect of initial concentration on adsorption capacity of the Ag-SAC toward DPS (b) (adsorbent = 0.5M-Ag-SAC, dosage = 0.8 mg mL^{-1}, temperature = 30 °C).

The equations of the three kinetic models are as follows:

Pseudo-first-order model:

$$\ln(q_e - q_t) = \ln(q_e) - k_1 t \tag{3}$$

Pseudo-second-order model:

$$\frac{t}{q_t} = \frac{1}{k_2 {q_e}^2} + \frac{t}{q_e} \tag{4}$$

Intra-particle diffusion model:

$$q_t = k_{int} t^{0.5} + C \tag{5}$$

where k_1 (min^{-1}) is the pseudo-first-order rate constant of adsorption. According to the intercept and slope of the linear plot, the values of q_e and k_1 can be calculated. k_2 (g mg^{-1} min^{-1}) is the pseudo-second-order rate constant of adsorption. k_{int} (mg g^{-1} min$^{-0.5}$) is the rate constant of intra-particle diffusion,

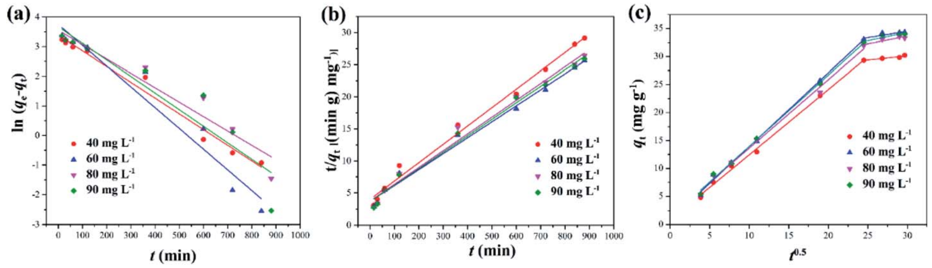

Fig. 7 Kinetic line for the adsorption of DPS by Ag-SAC based on pseudo-first-order model (a), pseudo-second-order kinetic model (b), intra-particle diffusion model (c) (adsorbent = 0.5M-Ag-SAC, temperature = 30 °C).

C is the intercept of the linear plot of q_t against $t^{0.5}$, which is proportional to the thickness of the boundary layer and can be used to judge whether intra-particle diffusion is the only rate-controlling step or not.

The results obtained by fitting the pseudo-first-order kinetic equation, the pseudo-second-order kinetic equation and the intra-particle diffusion models are shown in the Fig. 7 and Table 2. It can be seen from Table 2 that under different initial concentrations, the R^2 of the pseudo-second-order kinetic model are all larger than those of the pseudo-first-order kinetic model and the calculated equilibrium adsorption capacity $q_{\mathrm{e,cal}}$ is close to the experimentally determined value $q_{\mathrm{e,exp}}$. This demonstrates that the pseudo-second-order kinetic model can better describe the adsorption process than the first-order kinetic model, indicating that the adsorption of DPS by Ag-SAC may be dominated by chemical adsorption, which was contributed by the nano-silver.[40]

It can be seen from Fig. 7(c) and Table 2 that the adsorption process of DPS by Ag-SAC showed a multistage linear line. The first stage is related to external surface adsorption and instantaneous adsorption, which is mainly limited by film-diffusion. The second stage is the gradual adsorption stage where intra-particle diffusion became the main factor affecting the adsorption rate.[41] In this second stage, the pore volume of Ag-SAC became the most important determining element of adsorption capacity. As shown in Fig. 6(a), the quantity of 0.05M-Ag-SAC adsorption increased in the second stage. The adsorption quantity of 0.5M-Ag-SAC and 1M-Ag-SAC, on the other hand, did not increase appreciably. This is consistent with the fact that in Table 1, 0.05M-Ag-SAC has a greater pore volume. The first and second lines clearly do not pass through the origin ($C \neq 0$), showing that intra-particle diffusion was not the only rate-limiting process. The second stage C value grew dramatically, showing that the boundary layer effect has a considerable impact on the adsorption process in the second stage.

3.2.3 Adsorption equilibrium isotherms.

The equilibrium adsorption data of DPS on Ag-SAC was analysed using Langmuir and Freundlich isotherm models.

The Langmuir isotherm assumes a surface with homogeneous binding sites and equivalent sorption energies. It is expressed as:

$$\frac{C_{\mathrm{e}}}{q_{\mathrm{e}}} = \frac{1}{q_{\mathrm{m}} K_{\mathrm{L}}} + \frac{C_{\mathrm{e}}}{q_{\mathrm{m}}} \tag{6}$$

where q_{m} (mg g^{-1}) and K_{L} (L mg^{-1}) are Langmuir constants related to adsorption capacity and rate of adsorption, respectively.[39]

The Freundlich isotherm is an equation based on an exponential distribution of adsorption sites and energies. It is expressed as:

$$\ln(q_{\mathrm{e}}) = \ln(K_{\mathrm{F}}) + \frac{1}{n}\ln(C_{\mathrm{e}}) \tag{7}$$

where K_{F} (mg^2 g^{-1} L^{-1}) and n are Freundlich constants related to adsorption capacity and adsorption intensity, respectively.[39]

The fitting results of the Langmuir and Freundlich adsorption isotherm models as shown in Fig. 8(a) and (b). The parameters of the Langmuir and Freundlich adsorption isotherm models are shown in Table 3. According to Table 3, the R^2 of Langmuir adsorption isotherm model is as high as 0.999, and the q_{m} value calculated by the Langmuir equation (34.01 mg g^{-1}) was closer to the experimental value (34.34 mg g^{-1}). Therefore, the adsorption of DPS on Ag-SAC conformed to the Langmuir adsorption isotherm model, which belongs to the

Table 2 Kinetic parameters of pseudo-first-order model, pseudo-second-order model and intra-particle diffusion model

							Intra-particle diffusion model					
	Pseudo-first-order			Pseudo-second-order			Stage 1			Stage 2		
C_0	k_1	$q_{\mathrm{e,cal}}$	R^2	k_2	$q_{\mathrm{e,cal}}$	R^2	K_{int}	C	R^2	K_{int}	C	R^2
40	5.31×10^{-3}	29.57	0.978	2.06×10^{-4}	34.90	0.989	5.31×10^{-3}	29.57	0.978	2.06×10^{-4}	34.90	0.989
60	7.01×10^{-3}	42.27	0.943	1.70×10^{-4}	40.16	0.988	7.01×10^{-3}	42.27	0.943	1.70×10^{-4}	40.16	0.988
80	4.86×10^{-3}	34.94	0.928	1.85×10^{-4}	38.12	0.985	4.86×10^{-3}	34.94	0.928	1.85×10^{-4}	38.12	0.985
90	5.59×10^{-3}	39.23	0.865	1.83×10^{-4}	38.85	0.988	5.59×10^{-3}	39.23	0.865	1.83×10^{-4}	38.85	0.988

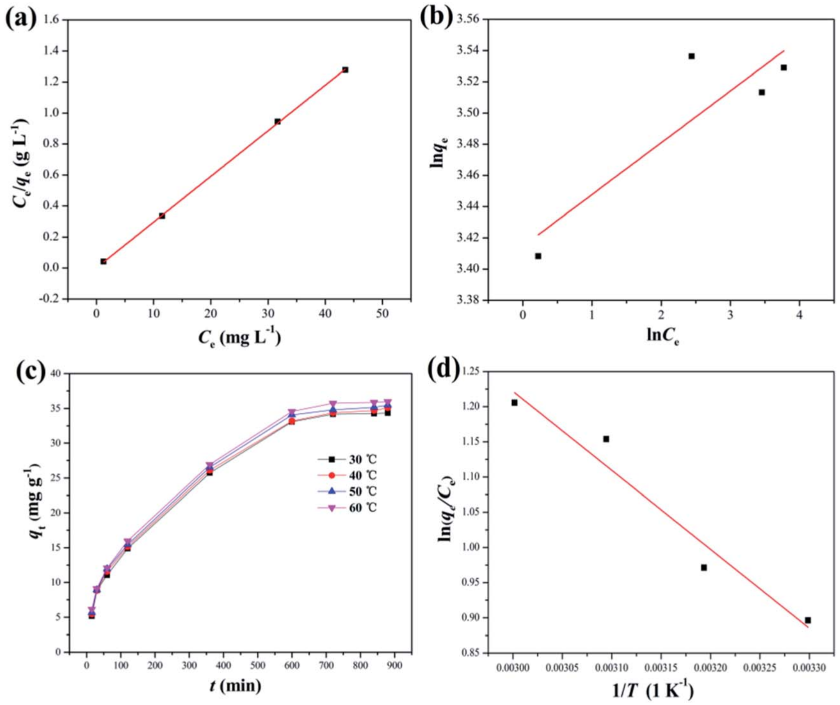

Fig. 8 Langmuir adsorption isotherm model (a) and Freundlich adsorption isotherm model (b) for the adsorption of DPS by Ag-SAC. (Adsorbent = 0.5M-Ag-SAC, temperature = 30 °C); effect of temperature on the adsorption (c) and Van't Hoff diagram (d) of the adsorption of DPS on Ag-SAC (adsorbent = 0.5M-Ag-SAC, C_0 = 60 mg L^{-1}, dosage = 0.8 mg mL^{-1}).

Table 3 Langmuir adsorption isotherm model, Freundlich adsorption isotherm model and thermodynamic parameters for the adsorption of DPS on 0.5M-Ag-SAC

Langmuir model					
q_m (mg g^{-1})		K_L (L mg^{-1})			R^2
34.01		10.39			0.999
Freundlich model					
K_F (mg g^{-1})		n			R^2
30.41		30.16			0.690
Adsorption thermodynamics					
ΔS (J mol^{-1} K^{-1})	ΔH (kJ mol^{-1})	ΔG (kJ mol^{-1})			
		30 °C	40 °C	50 °C	60 °C
0.04	9.33	−2.26	−2.56	−3.10	−3.34

single-layer adsorption, and the adsorption sites were uniformly distributed on the surface of Ag-SAC.[42]

3.2.4 **Adsorption thermodynamics.** Fig. 8(c) depicts the effect of temperature on the adsorption of DPS on Ag-SAC. The adsorption capacity increased from 34.34 mg g^{-1} to 35.96 mg g^{-1} with increasing temperature, indicating that the adsorption of DPS by Ag-SAC is an endothermic process.

The thermodynamic parameter values of Gibbs free energy (ΔG), enthalpy (ΔH), and entropy (ΔS) variations were calculated by using eqn (8)–(10).[43]

$$\ln(K_G) = \frac{\Delta S}{R} - \frac{\Delta H}{RT} \tag{8}$$

$$\Delta G = -RT\ln(K_G) \tag{9}$$

$$K_G = \frac{q_e}{C_e} \tag{10}$$

where T and K_G are the solution temperature and adsorption equilibrium constant, respectively. The values of ΔS and ΔH can be calculated from the intercept and slope of the Van't Hoff diagram as shown in Fig. 8(d). As shows in Table 3, the ΔH is positive, which indicated that the adsorption of DPS by Ag-SAC is an endothermic reaction. The positive values of ΔS suggest that the solid/liquid interface adsorbate concentration increases during adsorption.[44] The positive values of ΔH and ΔS further verified that the adsorption mechanism is chemical.[42] The adsorption process spontaneity and feasibility are indicated by a negative value of ΔG.[45] The value of ΔG tends to decrease from −2.26 kJ mol^{-1} to −3.34 kJ mol^{-1} as the temperature rises, which implies the facilitation of adsorption at higher temperature.[44]

3.2.5 **Sulfur mustard simulant adsorption mechanism by Ag-SAC.** The adsorption mechanism of DPS by Ag-SAC is a mixed synergistic process that includes chemical adsorption and physical adsorption. The chemical adsorption mechanism of DPS by Ag-SAC can be explained by the hard and soft acid–

base (HSAB) theory. As shows in Fig. 9, the chemical adsorption mechanism mainly involves the direct interaction between silver cation and sulfur atom (S–Ag) and the interaction between hard acid and hard base (S–H).[41] According to the HSAB theory, whether stable interaction can be formed between acids and bases is determined by their hardness. DPS is a kind of Lewis base organic sulfide,[41,46] and the sulfur atoms of DPS have two pairs of lone electrons: a π-lone pair electron and a σ-lone pair electron.[47] This electron configuration of DPS means that it can act as a hard or soft base. The silver cation formed on the surface of Ag-SAC is a soft acid. According to the HSAB theory, the adsorption of DPS by SAC is formed by the direct interaction between silver cation and sulfur atoms (S–Ag). In the process of S–Ag interaction, the π-lone pair electrons of sulfur atoms combine with silver ions to form an interaction.[41] In addition, $AgNO_3$ impregnation increased the surface acidity of Ag-SAC. According to the HSAB theory, the hard acidic sites of Ag-SAC can interact with the σ-lone pair electrons of S atom, which will form S–H enhance the adsorption of DPS.[41] According to the results of adsorption kinetics, the whole adsorption process is divided into two stages. In the first stage of adsorption, DPS interacts with the silver cation of Ag-SAC to form a stable S–Ag interaction. At the same time, DPS is adsorbed by the acidic sites on the Ag-SAC surface due to the S–H interaction. As shown in Fig. 7(c) and Table 2, the higher adsorption rate at this stage is attributed to the film-diffusion which leads to the rapid diffusion and coverage of DPS molecules on the pore surface. The second stage of adsorption is the gradual filling of pores by free DPS molecules, which is physical. The adsorption rate of this stage is controlled by intra-particle diffusion.

3.2.6 Antibacterial properties of Ag-SAC. As shown in Fig. 10, *Escherichia coli* (*E. coli*) was selected to evaluate the antibacterial activity of SAC and Ag-SAC, and the calculated results are listed in Table 4. It can be seen from Table 4 that the antibacterial rate of pristine SAC was less than 70%, indicating a poor antibacterial property, while Ag-SAC showed good antibacterial activity against *E. coli*, and the antibacterial rate was more than 99.28%. The antibacterial property of Ag-SAC can be attributed to the loading of nano-silver on the surface of Ag-SAC with intriguing antibacterial and bactericidal property. When silver ions contact with bacteria, they can destroy the cell wall and cytoplasmic membrane of bacteria, resulting in the easy penetration of bacteria by silver ions.[48] The absorbed silver ion can not only further destroy the cell membrane, but also make the bacteria unable to reproduce by interacting with sulfur and phosphorus in deoxyribonucleic acid.[48]

3.3 Performances of composite fabric with Ag-SAC

In order to evaluate the effect of Ag-SAC in the composite fabrics. The 0.5M-Ag-SAC was selected as the adsorbent to fabricated a composite fabric. The WVP of composite fabric was tested according to the Chinese standard GB/T12704.2-2009. Under the test conditions of 38 °C and 90% RH, the composite fabric was fixed at the mouth of the moisture-permeable cup, which contained distilled water. The WVP of the composite fabric is calculated according to the mass change of the moisture permeable cup. As a result, the WVP of the composite fabric was as high as 3000 $g\ m^{-2}$ per day, which indicates that the composite fabric meets the requirements of water vapor permeability (>2500 $g\ m^{-2}$ per day) according to Chinese standard: GB/T 21980-2017 General technical specification for sportswear and protecting suits.

Mover, the washing resistance fastness performance of composite fabric was also tested according to Chinese standard

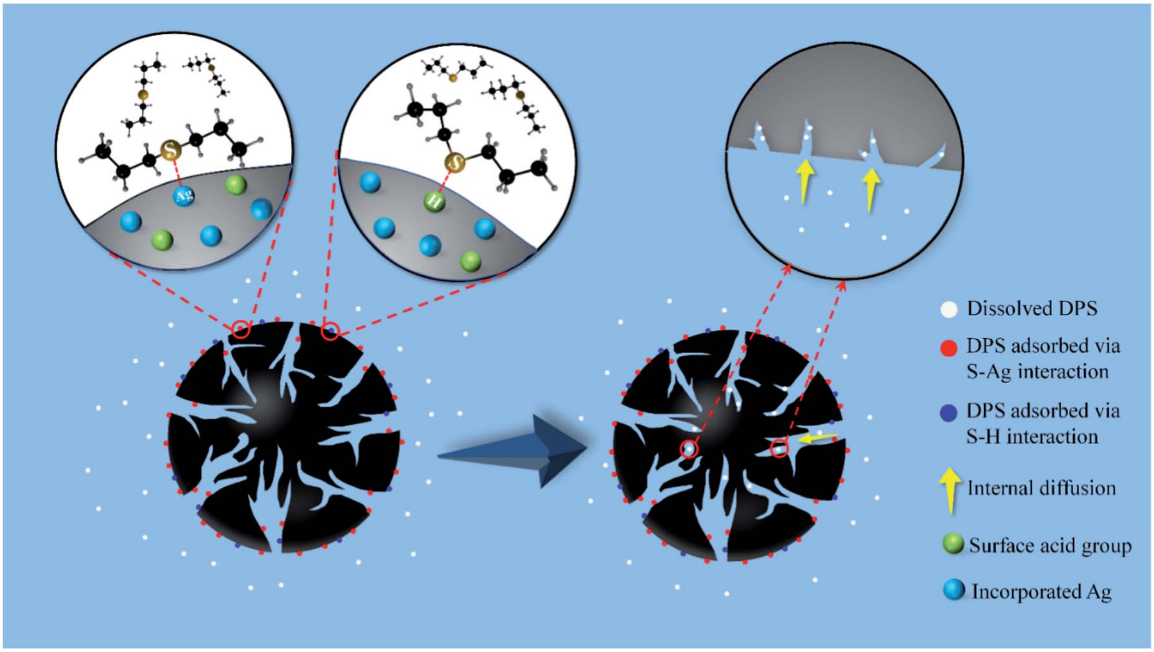

Fig. 9 The mechanism of DPS adsorption by Ag-SAC.

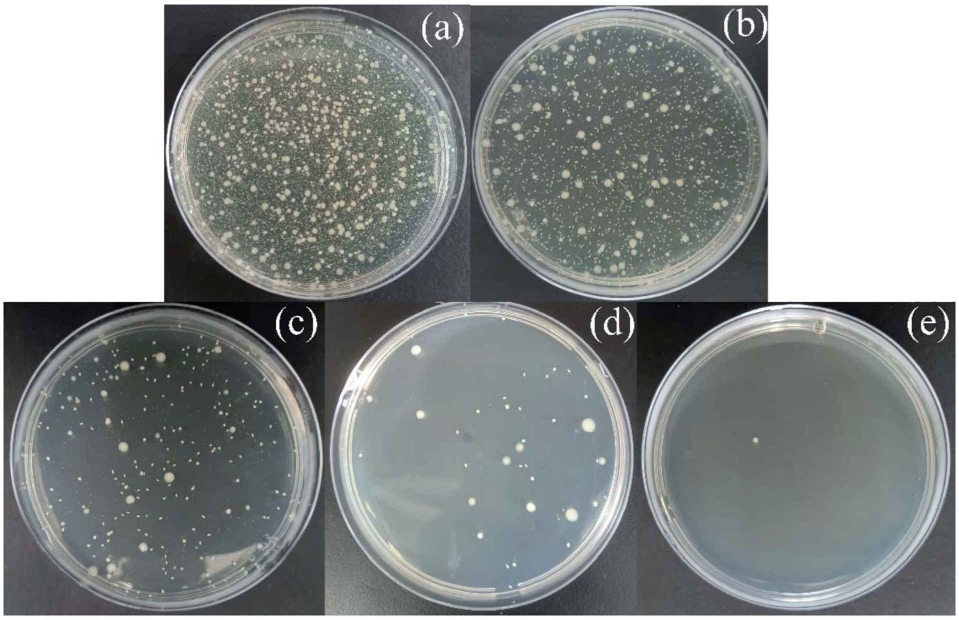

Fig. 10 Determination of antibacterial activity of empty control (a), SAC (b), 0.05M-Ag-SAC (c), 0.5M-Ag-SAC (d) and 1M-Ag-SAC (e).

Table 4 Antibacterial properties of SAC and Ag-SAC

Samples	Count of *E. coli* bacterial colonies (cfu ml^{-1})	Ratio of antibacterial activity (%)
Empty control	21050	—
SAC	6640	68.46
0.05M-Ag-SAC	152	99.28
0.5M-Ag-SAC	41	99.81
1M-Ag-SAC	1	99.99

GB/T 29255-2012. The composite fabric with Ag-SAC was put into the washing cup, which contained detergent and 10 steel beads. Then, the cup was put into the washing equipment and washed for 30 min at 40 °C. The bonding performance between Ag-SAC and fabric was characterized by the elution rate of Ag-SAC. As a result, the Ag-SAC elution rate of composite fabric is 0.128%. After five test cycles, the elution rate was 1.042%, indicating that the bonding of Ag-SAC with fabric was satisfactory.

4 Conclusions

In conclusion, the Ag-SAC composites were prepared by loading nano-silver on the surface of SAC through an excessive impregnation method. The resulting Ag-SAC composites exhibited good DPS (a selected sulfur mustard simulant) adsorption capacity and satisfactory antibacterial capabilities. According to the results of the kinetic model, isotherm model, and thermodynamic analysis, it was found that the adsorption of DPS by Ag-SAC was mainly a chemical adsorption process. To clarifies the adsorption mechanism of DPS by Ag-SAC, two reasonable adsorption processes have been proposed: (i) the direct interaction between silver cation and sulfur atom (S–Ag); (ii) the interaction between acid and base (S–H). Moreover, the antibacterial activity test revealed that Ag-SAC has good antibacterial activity, with an antibacterial rate over 99.28% against *E. coli*. Owing to an improved chemical warfare agent simulant adsorption capacity and good antibacterial capability, the Ag-SAC composites could be considered as a promising candidate for the development of next generation of breathable biochemical protective clothing.

Conflicts of interest

There are no conflicts to declare.

Acknowledgements

The work was financially supported by the Postgraduate Research & Practice Innovation Program of Jiangsu Province (KYCX202833), the National Natural Scienece Foundation of China (52003125), the Natural Science Foundation of Jiangsu Province (BK20200968) and the Natural Science Foundation of the Higher Education Institutions of Jiangsu Province (20KJB540001), the College Student Innovation Training Program of Jiangsu Province (202110304092Y).

References

1 H. Amini, M. Solaymani-Dodaran, B. Mousavi, S. N. A. Beladi, M. R. Soroush, J. Abolghasemi, A. Vahedian-Azimi, M. Salesi, P. C. Guest, A. Sahebkar and M. Ghanei, *JAMA Network Open*, 2020, **3**, e2028894.

2 M. Saito, N. Uchida, S. Furutani, M. Murahashi, W. Espulgar, N. Nagatani, H. Nagai, Y. Inoue, T. Ikeuchi, S. Kondo, H. Uzawa, Y. Seto and E. Tamiya, *Microsyst. Nanoeng.*, 2018, **4**, 17083.

3 R. S. Steinberg, M. Cruz, N. G. A. Mahfouz, Y. Qiu and R. H. Hurt, *ACS Nano*, 2017, **11**, 5670–5679.

4 L. Chen, L. Bromberg, J. A. Lee, H. Zhang, H. Schreuder-Gibson, P. Gibson, J. Walker, P. T. Hammond, T. A. Hatton and G. C. Rutledge, *Chem. Mater.*, 2010, **22**, 1429–1436.

5 M. Imran, N. Kumar, V. B. Thakare, A. K. Gupta, J. Acharya and P. Garg, *Anal. Bioanal. Chem.*, 2020, **412**, 1097–1110.

6 S. Wang, N. L. Pomerantz, Z. Dai, W. Xie, E. E. Anderson, T. Miller, S. A. Khan and G. N. Parsons, *Mater. Today Adv.*, 2020, **8**, 100085.

7 P. K. Sharma, V. V. Singh, N. K. Tripathi, M. Sathe, V. Verma, S. P. Sharma, L. N. S. Tomar, A. Chaturvedi, S. S. Yadav, V. B. Thakare, J. Acharya, A. K. Gupta and K. Ganesan, *Def. Sci. J.*, 2019, **69**, 577–584.

8 J. Krizkova and T. Vitvarova, *Chem. Listy*, 2017, **111**, 285–289.

9 S. S. Kiani, A. Farooq, M. Ahmad, N. Irfan, M. Nawaz and M. A. Irshad, *Environ. Sci. Pollut. Res.*, 2021, **28**, 60477–60494.

10 B. Cojocaru, S. Neatu, V. I. Parvulescu, V. Somoghi, N. Petrea, G. Epure, M. Alvaro and H. Garcia, *ChemSusChem*, 2009, **2**, 427–436.

11 J. Claudot, E. Soubeyrand-Lenoir and G. Maurin, *Appl. Surf. Sci.*, 2021, **538**, 148047.

12 J. Claudot, E. Soubeyrand-Lenoir and G. Maurin, *Appl. Surf. Sci.*, 2021, **551**, 149443.

13 S. Fichtner, J. Hofmann, A. Moller, C. Schrage, J. M. Giebelhausen, B. Bohringer and R. Glaser, *J. Hazard. Mater.*, 2013, **262**, 789–795.

14 J. A. Arcibar-Orozco, D. A. Giannakoudakis and T. J. Bandosz, *Chem. Eng. J.*, 2016, **303**, 123–136.

15 B. Maddah, J. Shamsi, M. J. Barsang and M. Rahimi-Nasrabadi, *Spectrochim. Acta, Part A*, 2015, **142**, 220–225.

16 L. Bigiani, D. Zappa, D. Barreca, A. Gasparotto, C. Sada, G. Tabacchi, E. Fois, E. Comini and C. Maccato, *ACS Appl. Mater. Interfaces*, 2019, **11**, 23692–23700.

17 V. V. Singh, B. Jurado-Sanchez, S. Sattayasamitsathit, J. Orozco, J. X. Li, M. Galarnyk, Y. Fedorak and J. Wang, *Adv. Funct. Mater.*, 2015, **25**, 2147–2155.

18 X. D. Wang, N. L. Zhou, J. Yuan, W. Y. Wang, Y. D. Tang, C. Y. Lu, J. Zhang and J. Shen, *J. Mater. Chem.*, 2012, **22**, 1673–1678.

19 P. M. Liu, T. Huang, P. S. Liu, S. F. Shi, Q. Chen, L. Li and J. Shen, *J. Colloid Interface Sci.*, 2016, **480**, 91–101.

20 M. Q. Wang, H. M. Zhu and J. Shen, *New J. Chem.*, 2021, **45**, 6895–6903.

21 G. Y. Zhang, R. Cheng, J. W. Yan, Y. Xiao, C. A. F. Zang and Y. Zhang, *Polym. Test.*, 2021, **100**, 107235.

22 R. N. Saladi, E. Smith and A. N. Persaud, *Clin. Exp. Dermatol.*, 2006, **31**, 1–5.

23 P. Asha, M. Sinha and S. Mandal, *RSC Adv.*, 2017, **7**, 6691–6696.

24 J. Park, M. Agrawal, D. F. S. Gallis, J. A. Harvey, J. A. Greathouse and D. S. Sholl, *Phys. Chem. Chem. Phys.*, 2020, **22**, 6441–6448.

25 A. El-Hendawy, *Carbon*, 2003, **41**, 713–722.

26 E. Altintig and S. Kirkil, *J. Taiwan Inst. Chem. Eng.*, 2016, **63**, 180–188.

27 A. M. Aljeboree, A. N. Alshirifi and A. F. Alkaim, *Arabian J. Chem.*, 2017, **10**, S3381–S3393.

28 W. M. Daoush, B. K. Lim, D. H. Nam and S. H. Hong, *J. Exp. Nanosci.*, 2014, **9**, 588–596.

29 Y. T. Xie, S. H. Ouyang, D. P. Wang, W. Y. Lee and H. H. Fong, *J. Mater. Sci.*, 2020, **55**, 15908–15918.

30 C. L. Tang, D. M. Hu, Q. Q. Cao, W. Yan and B. Xing, *Appl. Surf. Sci.*, 2017, **394**, 457–465.

31 R. Das, V. S. Sypu, H. K. Paumo, M. Bhaumik, V. Maharaj and A. Maity, *Appl. Catal., B*, 2019, **244**, 546–558.

32 M. H. Kim, D. Cho, O. H. Kwon and W. H. Park, *J. Alloys Compd.*, 2018, **735**, 2670–2674.

33 H. Ortiz-Ibarra, R. Torres-Vitela, S. Gomez-Salazar, N. Casillas, C. P. de Leon and F. C. Walsh, *J. Solid State Electrochem.*, 2018, **22**, 749–759.

34 R. Vinodh and D. Sangeetha, *J. Mater. Sci.*, 2012, **47**, 852–859.

35 J. S. Choi, H. Lee, Y. K. Park, S. J. Kim, B. J. Kim, K. H. An, B. H. Kim and S. C. Jung, *J. Nanosci. Nanotechnol.*, 2016, **16**, 4493–4497.

36 Y. Zhao, Z. Q. Wang, X. Zhao, W. Li and S. X. Liu, *Appl. Surf. Sci.*, 2013, **266**, 67–72.

37 M. Sevilla and A. B. Fuertes, *ACS Nano*, 2014, **8**, 5069–5078.

38 W. Y. Qu, T. Yuan, G. J. Yin, S. A. Xu, Q. Zhang and H. J. Su, *Fuel*, 2019, **249**, 45–53.

39 Q. X. Liu, Y. R. Zhou, M. Wang, Q. Zhang, T. Ji, T. Y. Chen and D. C. Yu, *Adsorpt. Sci. Technol.*, 2019, **37**, 312–332.

40 Q. X. Liu, S. Q. Hu, Z. L. Yang, X. Y. Zhang and J. L. Ge, *Materials*, 2019, **12**, 4106.

41 R. Neubauer, M. Husmann, C. Weinlaender, N. Kienzl, E. Leitner and C. Hochenauer, *Chem. Eng. J.*, 2017, **309**, 840–849.

42 M. M. Weng, Q. Zhu, A. W. Wang, G. J. Liu and H. H. Huang, *J. Mater. Sci.*, 2020, **55**, 15797–15812.

43 S. Gao, W. Zhang, Z. An, S. Kong and D. Chen, *Adsorpt. Sci. Technol.*, 2019, **37**, 185–204.

44 M. Ghaedi, Z. Andikaey, A. Daneshfar, T. Akbari and R. Sahraei, *Desalin. Water Treat.*, 2014, **52**, 5494–5503.

45 M. A. Salem, R. G. Elsharkawy, M. I. Ayad and M. Y. Elgendy, *J. Sol-Gel Sci. Technol.*, 2019, **91**, 523–538.

46 X. W. Chu, P. J. Guo, Y. Pei, S. R. Yan, H. R. Hu, M. H. Qiao, K. N. Fan, B. N. Zong and X. X. Zhang, *J. Phys. Chem. C*, 2007, **111**, 17535–17540.

47 J. J. Gao, H. Q. Li, H. X. Zhang, Y. Z. Lu, H. Meng and C. X. Li, *Ind. Eng. Chem. Res.*, 2012, **51**, 4682–4691.

48 I. X. Yin, J. Zhang, I. S. Zhao, M. L. Mei, Q. L. Li and C. H. Chu, *Int. J. Nanomed.*, 2020, **15**, 2555–2562.